

3D magnetised jet break-out from neutron-star binary merger ejecta: afterglow emission from the jet and the ejecta

Antonios Nathanail¹, Ramandeep Gill^{2,3}, Oliver Porth⁴, Christian M. Fromm^{1,5}, and Luciano Rezzolla^{1,6,7}

¹*Institut für Theoretische Physik, Goethe Universität Frankfurt, Max-von-Laue-Str.1, 60438 Frankfurt am Main, Germany*

²*Department of Physics, The George Washington University, Washington, DC 20052, USA*

³*Department of Natural Sciences, The Open University of Israel, 1 University Road, PO Box 808, Raanana 4353701, Israel*

⁴*Astronomical Institute Anton Pannekoek, Universeit van Amsterdam, Science Park 904, 1098 XH, Amsterdam, The Netherlands*

⁵*Max-Planck-Institut für Radioastronomie, Auf dem Hügel 69, D-53121 Bonn, Germany*

⁶*Helmholtz Research Academy Hesse for FAIR, Max-von-Laue-Str. 12, 60438 Frankfurt am Main, Germany*

⁷*School of Mathematics, Trinity College, Dublin 2, Ireland*

1 February 2021

ABSTRACT

We perform three-dimensional (3D) general-relativistic magnetohydrodynamic simulations to model the jet break-out from the ejecta expected to be produced in a binary neutron-star merger. The structure of the relativistic outflow from the 3D simulation confirms our previous results from 2D simulations, namely, that a relativistic magnetized outflow breaking out from the merger ejecta exhibits a hollow core of $\theta_{\text{core}} \approx 4^\circ$, an opening angle of $\theta_{\text{jet}} \gtrsim 10^\circ$, and is accompanied by a wind of ejected matter that will contribute to the kilonova emission. We also compute the non-thermal afterglow emission of the relativistic outflow and fit it to the panchromatic afterglow from GRB170817A, together with the superluminal motion reported from VLBI observations. In this way, we deduce an observer angle of $\theta_{\text{obs}} = 35.7^\circ_{-2.2}^{+1.8}$. We further compute the afterglow emission from the ejected matter and constrain the parameter space for a scenario in which the matter responsible for the thermal kilonova emission will also lead to a non-thermal emission yet to be observed.

Key words: MHD, gamma-ray burst: general, stars: neutron

1 INTRODUCTION

Binary neutron-star (BNS) mergers offer a rich variety of observables, from the gravitational waves (GWs) and kilonova emission powered by the neutron rich ejected matter to the prompt emission from an ultra-relativistic jet and its late-time afterglow signal. A short gamma-ray burst (GRB) is expected after the jet breaks out from the BNS merger ejecta. The first ever detection of GWs from a BNS merger, GW170817 (The LIGO Scientific Collaboration & The Virgo Collaboration 2017), was accompanied by a number of electromagnetic signals (The LIGO Scientific Collaboration et al. 2017): a coincident detection of a short GRB, GRB170817A (Savchenko et al. 2017; Goldstein et al. 2017), a quasi-thermal kilonova detection from the first day till several days later (Arcavi et al. 2017; Nicholl et al. 2017; Chornock et al. 2017; Cowperthwaite et al. 2017; Villar et al. 2017), and a non-thermal afterglow emission that appeared in the X-rays nine days after the merger (Troja et al. 2017), and in the optical, and radio bands more than fifteen days post-merger (Hallinan et al. 2017). The latest afterglow observations were in the X-rays at 743 and 940 days after the merger (Hajela et al. 2019; Makhathini et al. 2020).

To understand the outflow energetics and its structure, the af-

terglow was extensively studied from the continuous brightening of the flux, with its peculiar shallow rise to the peak at $t_{\text{pk}} \approx 150$ d post-merger (Lyman et al. 2018; Margutti et al. 2018; Mooley et al. 2018a), to well into the late-time decay phase after the lightcurve peak (Alexander et al. 2018; Troja et al. 2019). Several works developed simplified semi-analytical models and employed two-dimensional (2D) nonlinear numerical simulations to understand the shallow rise of the afterglow lightcurve before its peak. Two distinct types of outflow structures were tested against the observations: one featured a “structured jet”, with a polar structure and a narrow relativistic core surrounded by low-energy wings (e.g., Troja et al. 2017, 2018; Gill & Granot 2018; D’Avanzo et al. 2018; Margutti et al. 2018; Lazzati et al. 2018; Lamb & Kobayashi 2018; Pozanenko et al. 2018; Beniamini & Nakar 2019), and the second featured a “cocoon”, namely, a wide-angle outflow expanding quasi-spherically, with a radial velocity stratification (e.g., Kasliwal et al. 2017; Gill & Granot 2018; Gottlieb et al. 2018a; Salafia et al. 2018; Mooley et al. 2018a; Fraija & Veres 2018). The radio observation of an apparent superluminal motion of the flux centroid (Mooley et al. 2018b), together with a compact size (i.e., $\lesssim 2$ mas) of the outflow on the plane of the sky (Ghirlanda et al. 2019), favoured the structured jet model, that was needed to explain the afterglow

lightcurve and image properties near and after the peak (Lamb et al. 2018).

The details of the afterglow lightcurve (e.g., Beniamini et al. 2020a) and image properties depend mainly on the jet structure, the ambient rest-mass density and our line-of-sight. The structure of the jet, on the other hand, is determined already early on at the site where the jet is launched, which is expected to happen in the vicinity of a rotating black hole, but also through its interaction with the circumburst medium through which the jet is drilling a hole. Such a medium is composed of the matter ejected during the merger – either dynamically or secularly (see, e.g., Baiotti & Rezzolla 2017; Paschalidis 2017, for some reviews) – but also of the accretion torus that is formed when the merger remnant collapses to a black hole. Both of these components affects the jet’s structure and propagation.

Hydrodynamic jets have been studied analytically in a large number of recent works (Bromberg et al. 2011; Nakar & Piran 2017; Lazzati et al. 2018; Salafia et al. 2018) and numerically (Nagakura et al. 2014; Murguia-Berthier et al. 2014, 2016; Lamb & Kobayashi 2017; Duffell et al. 2015, 2018; Lazzati et al. 2017; Xie et al. 2018; Gottlieb et al. 2018b; Matsumoto & Masada 2019; Hamidani et al. 2020; Hamidani & Ioka 2020; Gottlieb et al. 2020a). On the other hand, studies of (MHD) jets in the context of short GRBs and produced after a BNS merger are considerably fewer (Kathirgamaraju et al. 2018; Bromberg et al. 2018; Geng et al. 2019; Fernández et al. 2019; Kathirgamaraju et al. 2019a; Sapountzis & Janiuk 2019; Nathanail et al. 2020; Gottlieb et al. 2020b). Yet, there are substantial differences between the properties of a hydrodynamic jet and of an MHD jet breaking out from the merger ejecta.

By carrying out a series of 2D of general-relativistic MHD (GRMHD) simulations that considered variations in the matter distribution around a black hole and its spin as well as the magnetic field geometry and energy, Nathanail et al. 2020 suggested that MHD jets have the following properties: (i) they have an intrinsic polar structure for the energy and velocity with a “hollow core” of $\theta_{\text{core}} \approx 4^\circ - 5^\circ$ (measured from the jet symmetry axis) and an opening angle of $\theta_{\text{jet}} \gtrsim 10^\circ$; (ii) they are followed by a disc wind with significant amounts of matter, which contributes to the overall ejected mass that follows a BNS merger; (iii) they naturally develop an angular (and radial) energy stratification by the interaction of the surrounding matter.

The afterglow of GRB170817A was analysed mainly by using numerical and semi-analytical models of hydrodynamic jets that best fit the afterglow data, and correspond to structured jets with a relativistic core of angular size $\theta_{\text{core}} \sim 3^\circ - 5^\circ$ (Resmi et al. 2018; Mooley et al. 2018b; Ghirlanda et al. 2019; Troja et al. 2019; Lamb et al. 2019; Beniamini et al. 2019; Gill et al. 2019b; Nakar & Piran 2020). However, in the case of an MHD jet, the opening angle is certainly very different (Kathirgamaraju et al. 2019a; Nathanail et al. 2020)¹, which would affect also the resulting viewing angle of the afterglow emission.

In this study we report three-dimensional (3D) GRMHD simulations to explore the structure of an MHD jet as it breaks out the merger ejecta. The jet is launched self-consistently after the massive remnant, produced from the BNS merger, collapses to a black hole. Overall, our simulations confirm our previous results on the intrinsic properties of MHD jets that were found from 2D GRMHD simulations (Nathanail et al. 2020). We further explore the MHD wind that

accompanies the jet, another source of ejected mass, by calculating its non-thermal afterglow emission and investigating possibilities for its observational signature.

This paper is organised as follows: in Section 2 we present the numerical setup and the main results for the structure of the 3D MHD jet. In Section 3, we discuss the method used to compute the afterglow emission and present the resulting lightcurves. The details of the ejected mass produced by the MHD wind from the accretion disc are presented in Section 4, together with the non-thermal observable properties of this component. Finally, we summarise and present a discussion about the results in Section 5.

2 MHD JETS IN 3D

For our 2D and 3D simulations, we employ BHAC to solve the general-relativistic MHD equations in a Kerr background space-time (Porth et al. 2017; Olivares et al. 2019), in the ideal-MHD limit (Harutyunyan et al. 2018). To model the torus around the compact remnant together with the ejected matter that followed a BNS merger, we follow the setup introduced in Nathanail et al. (2019). We consider a non self-gravitating torus with initial size $r_{\text{in}} = 6M = 23.8 \text{ km}$ and $r_{\text{max}} = 14.3M = 56.7 \text{ km}$ (Fishbone & Moncrief 1976; Abramowicz et al. 1978) around a remnant black hole of mass $M = 2.7M_\odot$, with a dimensionless spin of $a := J/M^2 = 0.9375$. In our previous study we showed that the spin parameter does not have a strong impact on the jet structure, more specifically lower spins generate jets that break out from the merger ejecta (Nathanail et al. 2020). We recall that numerical-relativity simulations reveal that the BH produced from a BNS merger is expected to have a dimensionless spin $a \sim 0.7 - 0.9$ (Kastaun et al. 2013; Bernuzzi et al. 2014; Baiotti & Rezzolla 2017). We should remark that adopting a low-spin prior for GW170817 implies that the most realistic value for the dimensionless spin is $a \simeq 0.8$ (Kastaun et al. 2013; Bernuzzi et al. 2014). In turn, assuming that the power in the jet scales quadratically with a – as in the Blandford-Znajek mechanism (Blandford & Znajek 1977) – reveals that the jet power in our simulations is overestimated by $\sim 23\%$, which is well within the systematic error budget of our modelling. More importantly, the structure of the jet is not significantly affected by the exact value of a as long as the jet energy is considerably larger than that in the ejecta. The jet structure is indeed affected in cases where the jet barely makes out of the ejecta (e.g., Urrutia et al. 2020, for hydrodynamical simulations of jet breakout for different jet powers and durations).

The initial matter distribution has a radial extent of 1200 km, in order to account for the expanded torus, and also for the dynamically ejected matter during merger that has reached such a distance, since the launch of a relativistic jet from GW170817/GRB170817A is expected to be significantly later from merger after the remnant collapsed to a black hole, i.e., $\approx 1 \text{ s}$ (Margalit & Metzger 2017; Shibata et al. 2017; Rezzolla et al. 2018; Granot et al. 2017; Nathanail 2018b; Gill et al. 2019a; Beniamini et al. 2020b; Murguia-Berthier et al. 2020). The numerical domain has a radius of 10^4 km and initially all matter is bound with having zero radial velocity. Here we report a 3D simulation with effective resolution of 192^3 realised by three refinement levels and as a comparison, we report another two simulations performed in axisymmetry (2D) with a resolution of 1024×512 using three refinement levels.

An important point of the initial post-merger configuration is the non-empty funnel in the polar region, which is expected as a result of the dynamically ejected matter during the merger

¹ Note that weakly magnetized jets do not show the characteristic structure of MHD jets (Gottlieb et al. 2020b).

(Sekiguchi et al. 2016; Foucart et al. 2016; Radice et al. 2016; Bovard et al. 2017; Dietrich et al. 2017; Fujibayashi et al. 2018; Most et al. 2019). To model this, we fill the polar region with matter that has a 2.5 orders of magnitude less rest-mass density than the maximum rest-mass density of the torus and its radial profile scales like $r^{-1.5}$, $\rho_{\text{polar}}(r) = 10^{-2.5} \times \rho_{\text{max}}(r/r_{\text{max}})^{-1.5}$. Initially, this matter distribution has a zero radial velocity, since the relative average velocity of these ejecta is $\langle \beta \rangle := \langle v \rangle / c \sim 0.1 - 0.2$ (Rezzolla et al. 2010; Siegel et al. 2014; Sekiguchi et al. 2016; Foucart et al. 2016; Radice et al. 2016; Bovard et al. 2017; Dietrich et al. 2017; Fujibayashi et al. 2018; Most et al. 2019) and it is considerably slower than the generated relativistic outflow. Given that our focus here is the angular structure of the relativistic jet as it traverses the dynamical region – which is most sensitive to the density profile of the ejecta – we believe that this is reasonable approximation. On the other hand, a sub-relativistic velocity of the ejecta is important for calculating, e.g., the jet breakout timescale, as indicated by some recent analytic work (Hamidani et al. 2020).

During merger, the initial magnetic field of the two neutron stars is amplified in the first milliseconds via instabilities such as the Kelvin-Helmholtz or the magnetorotational (MRI), yielding a magnetic energy for the remnant $> 10^{50}$ erg, with a dominant toroidal component with a factor of ≈ 3 larger than the poloidal one (Giacomazzo et al. 2015; Palenzuela et al. 2015; Kiuchi et al. 2015, 2018). Thus the initial magnetic energy is $\leq 10^{50}$ erg, which imposes a magnetisation in the torus. The magnetic field generated by these instabilities is mostly poloidal and on small scales (Siegel et al. 2013), although also a global toroidal component with a similar magnetic energy is achieved ≈ 20 ms after the merger (Ciolfi et al. 2017; Most et al. 2019).

The mass in the torus is $M_{\text{tor}} \approx 0.1 M_{\odot}$ whereas the mass surrounding the torus, which initially is bound for all simulations, is $M_{\text{surrounding}} = 0.02 M_{\odot}$. We initialise a poloidal nested-loop magnetic field, together with a toroidal component that traces the fluid pressure, with the desired ratio of ≈ 3 in the corresponding magnetic energies. The details of the models presented in this study are shown in Table 1.

In our previous study we explored a wide range of parameters for the initial configuration by varying the initial torus size and shape, the magnetic field strength and ratio (poloidal to toroidal component), and the BH spin (Nathanail et al. 2020). The main results of that parameter study was that the MHD jets, breaking out from the BNS merger ejecta, have several intrinsic properties that depend insignificantly on the initial configuration: (i) they have an intrinsic polar structure for the energy and velocity with a “hollow core” of $\theta_{\text{core}} \approx 4^{\circ} - 5^{\circ}$ (measured from the jet symmetry axis) and an opening angle of $\theta_{\text{jet}} \gtrsim 10^{\circ}$; (ii) they are followed by a disc wind with significant amounts of matter, which contributes to the overall ejected mass that follows a BNS merger; (iii) they naturally develop an angular (and radial) energy stratification. All our simulations were performed in 2D, thus there was a need to continue this analysis in three dimensions to explore the impact of known instabilities that occur in 3D. One example is the “plug” of heavy material that accumulates on the jet head in 2D (Lazzati et al. 2010; Mizuta & Ioka 2013; Gottlieb et al. 2018a), but disappears in 3D. Another important aspect is whether the hollow core angular structure found in 2D survives against potential 3D jet instabilities like the kink (e.g. Moll et al. 2008; McKinney & Blandford 2009; Mizuno et al. 2012).

From the initial setup, the MRI develops inside the torus and drives accretion onto the black hole (more details in the Appendix A). As matter plunges onto the black hole it contributes to the ac-

cumulation of magnetic flux over the event horizon and a magnetically dominated funnel starts to emerge. At the same time, magnetic pressure drives an MHD wind from the outer layers of the torus. Subsequently, an MHD jet is launched along the axis of rotation of the black hole while it is confined by the torus and the surrounding high rest-mass density material. After launch the jet starts to accelerate and finally breaks out of the merger ejecta. At such times, the outflow can be clearly defined by two distinguishable components: the relativistic jet with bulk Lorentz factor $\Gamma \gg 1$ and the MHD wind (ejecta) with velocities that span from $0.1 - 0.9 c$. Most of this mass in the latter component is sub-relativistic and only a tail of this acquires high velocities. Such a fast-moving tail component has been indicated and discussed in BNS merger simulations (Hotokezaka et al. 2013, 2018; Bauswein et al. 2013; Radice et al. 2018). During the jet formation and acceleration we have not detected the development of a kink instability; this may be due to the strong poloidal magnetic field employed in the initial configuration. It is possible, however, that such instability will develop on timescales longer than those explored with our simulations and if a strong toroidal component has developed. Indeed, following Appl et al. (2000), we can obtain approximate estimates of the growth-time of the kink instability τ_{kink} at different times during the simulation, finding that $\tau_{\text{kink}} \sim 39$ ms after 15 ms in the evolution and that that $\tau_{\text{kink}} \sim 220$ ms after 20 ms. Clearly, these timescales are always larger than the simulation time (≈ 20 ms).

In Fig. 1 we present the resulting structure of the MHD jet post break-out from the matter distribution. Both panels show four consecutive times for the development of the shape of the jet and clear distinction of the MHD ejecta component. Simulation data are averaged in the azimuthal ϕ direction. In the upper panel we show the Lorentz factor of the outflow, where it is clearly seen that the jet poses a slow moving core within an angle of $\theta_{\text{core}} \approx 4^{\circ}$, this confirms our previous results from 2D simulations. More specifically, the relativistic jet is confined to polar angles $\theta_{\text{core}} \lesssim \theta \lesssim \theta_{\text{jet}}$, where $\theta_{\text{jet}} \approx 10^{\circ} - 15^{\circ}$. The high end of θ_{jet} range is acquired as the flow advances in radius $\approx 4 \times 10^8$ cm (left-most plot of the upper panel in Fig. 1). Such an opening angle is also inferred from numerical-relativity simulations where the only the starting point for the launching of such a jet is reached (Rezzolla et al. 2011; Kiuchi et al. 2014; Dionysopoulou et al. 2015; Kawamura et al. 2016; Ruiz et al. 2016), and there is a need to combine such results with what we simulate here (Nathanail 2018a).

In the lower panels of Fig. 1 we present the rest-mass density distribution as the jet breaks out. In order to quantify how much matter becomes unbound, we use the Bernoulli criterion and assume a fluid element to be unbound if it has $hu_t \leq -1$, where h is the specific enthalpy of the fluid (Rezzolla & Zanotti 2013). The red solid line indicates the contour of $hu_t = -1$ that marks the boundary of the unbound mass, which means that all matter above the red solid line can be safely considered to be part either of the jet component or the ejecta component. We apply the Bernoulli criterion to measure the amount of unbound matter that passes through a 2-sphere of 1, 200 km and report it in the last two columns of Table 1, the actual amount of ejected mass and the fraction of the ejected mass with respect to the initial mass of the torus. The amount of the ejected mass for model MHD-3D-HB is 26.1% of the initial mass which is similar to what found from the 2D simulations².

² In our previous study due to the much larger evolution times from all the models reported there, the ejected matter was extracted after passing through a 2-sphere of 4, 000 km (Nathanail et al. 2020).

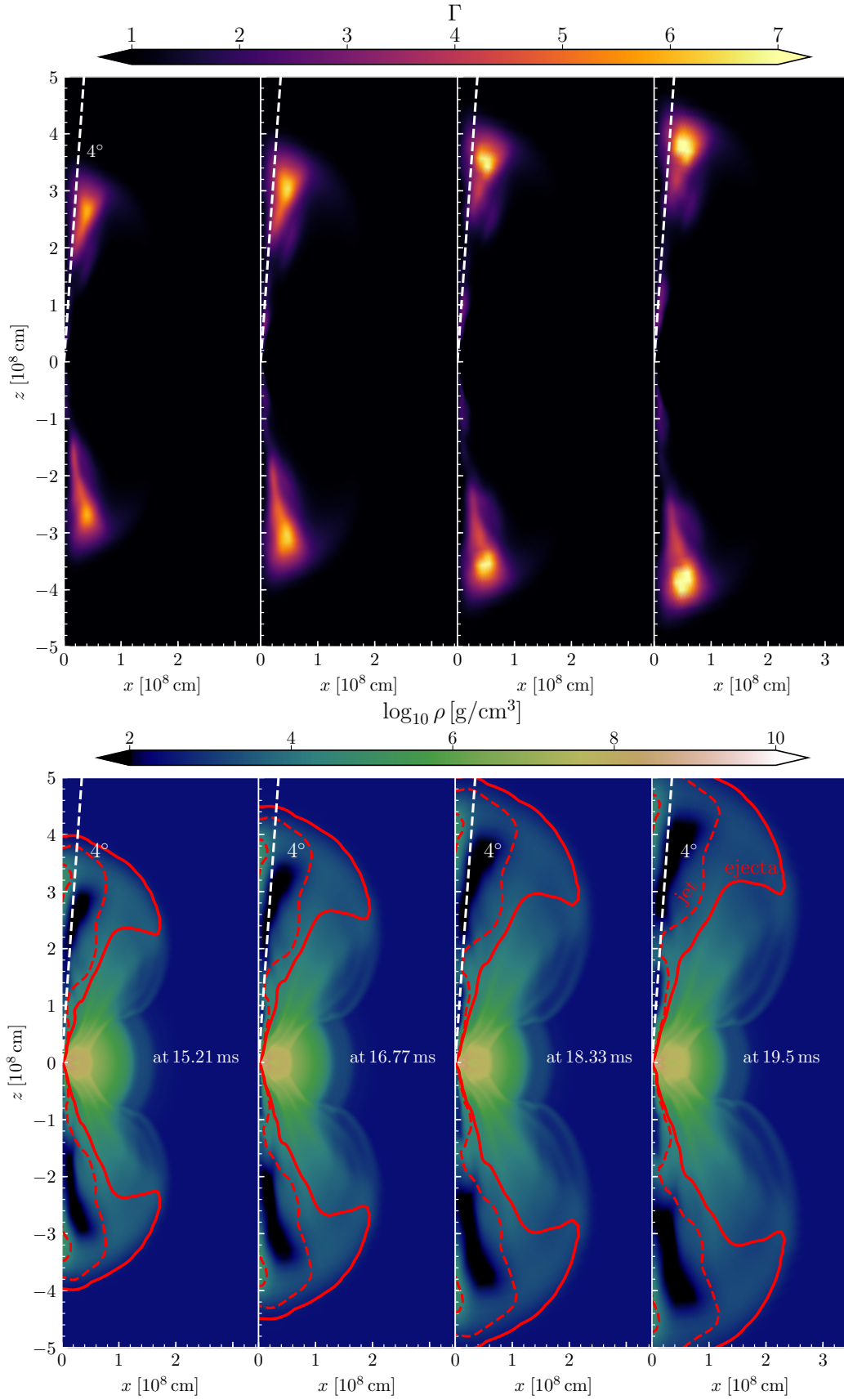


Figure 1. Lorentz factor (upper panels) and rest-mass density (lower panels) distribution for four consecutive snapshots azimuthally averaged. A cone with opening angle of 4° is indicated with a dashed white line to highlight the slow moving core. On the lower panels the red solid lines denote the contour of $hu_t = -1$ (gravitationally unbound), so that matter above such line is considered as merger ejecta, the red dashed lines denote the contour of $hu_t = -2.6$, inside this line matter has Lorentz factor $\Gamma > 2$, and is considered to be in the jet.

Table 1. Properties of the three MHD jets considered: magnetic energy (E_B), average magnetisation in the torus ($\bar{\sigma} := B^2/4\pi\rho$), maximum rest-mass density of the torus (ρ_{\max}), initial total mass ($M_{\text{tot}} = M_{\text{tor}} + M_{\text{surrounding}}$, where M_{tor} is the initial torus mass and $M_{\text{surrounding}} = 0.02M_{\odot}$ is the mass surrounding the torus which initially is bound and in all simulations), the unbound ejected mass at the end of the simulation (M_{ej}) and their ratio.

model	E_B [erg] 10^{49}	$\bar{\sigma}$ 10^{-6}	ρ_{\max} [g/cm ³] 10^{10}	M_{tot} [M_{\odot}]	M_{ej} [M_{\odot}]	$\frac{M_{\text{ej}}}{M_{\text{tot}}}$ %
MHD-3D-HB	10.0	3.9	45	0.109	0.027	26.1
MHD-2D-HB	9.0	0.065	2.0	0.144	0.038	27.1
MHD-2D-MB	1.2	0.036	1.5	0.108	0.014	14.1

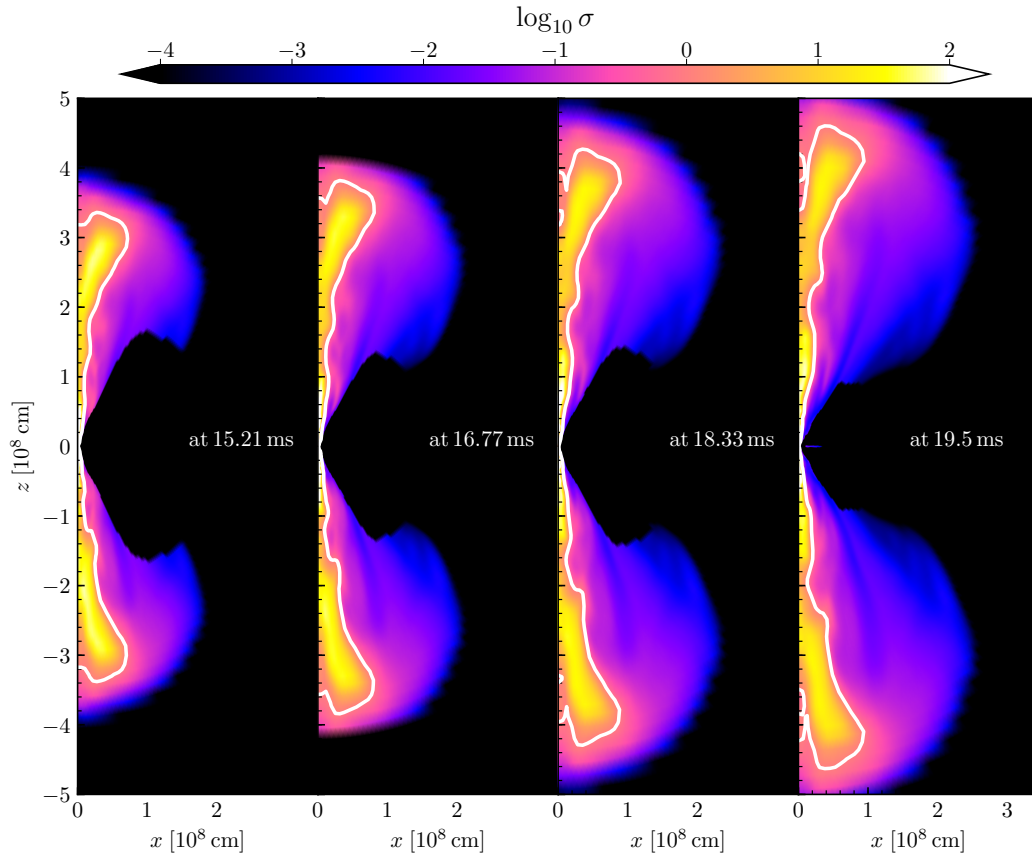


Figure 2. Magnetisation σ for four consecutive snapshots azimuthally averaged. The white solid lines denote the contour of $\sigma = 1$, the part of the outflow enclosed by the contour is highly magnetized and will experience efficient magnetic acceleration.

The red dashed line corresponds to a contour of $hu_t = -2.6$ (almost identical to the contour of $\Gamma = 2$ and of $\sigma = 1$, see below). We consider matter inside the red dashed line to be part of the jet whereas outside of this to be part of the ejecta. The fast-moving tail of the ejecta that reaches velocities of $\approx 0.87c$ lies closely outside the boundary of the jet. The outflow that breaks out from the merger ejecta is highly magnetized with magnetisation, the ratio of magnetic field to cold matter enthalpy densities, $\sigma = B^2/\rho c^2 > 10$. This is seen in Figure 2, where we azimuthally average the magnetisation of the outflow and also denote the $\sigma = 1$ contour by a white solid line.

At this stage it is expected that the jet has not fully undergone complete MHD acceleration, thus we obtain both the Lorentz factor straight from the simulation, Γ_{sim} , is the maximum Lorentz factor at a certain angle, as well as the terminal Lorentz factor, Γ_{∞} , expected

after MHD acceleration. It has been shown semi-analytically and numerically that a confined relativistic outflow highly magnetized (Fig. 2), can be efficiently accelerated and attain a Lorentz factor more than 50% μ , depending on the details of the solution (Vlahakis & Königl 2003a,b; Tchekhovskoy et al. 2008; Komissarov et al. 2009; Lyubarsky 2010a), where μ is the ratio of the total energy flux to mass flux. We calculate Γ_{∞} for the part of the outflow that passes radially $> 2 \times 10^8$ cm by averaging the energy-weighted μ over ϕ and time t (Kathirgamaraju et al. 2019a):

$$\Gamma_{\infty} = \frac{\int \mu T_t^r d\phi dt}{\int T_t^r d\phi dt}, \quad (1)$$

where T_t^r is the radial energy flux that comes from the stress-energy tensor (subtracting rest mass energy). The above estimation gives a measure of how a magnetically dominated outflow efficiently con-

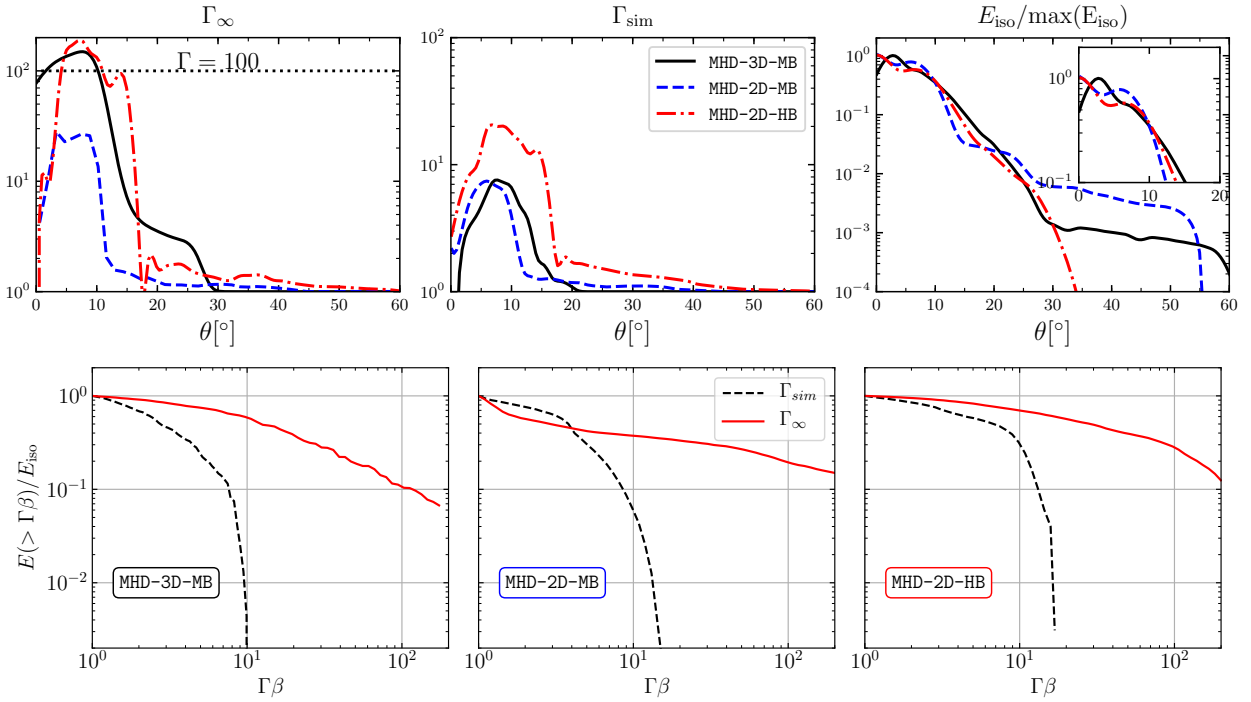


Figure 3. Left upper panel: Terminal Lorentz factor for the three models considered. Middle upper panel: Lorentz factor of the simulation, Right upper panel: the normalized energy distribution across θ , the in-box plot is a zoom in at small angles. Model MHD-3D-HB is shown in black solid lines, MHD-2D-HB in red dashed-dotted lines and MHD-2D-MB in blue dashed lines. Lower panels: Normalized energy distributions $E(> \Gamma\beta)/E_{\text{iso}}$ for the three models that is approximately obtained for all polar angles. The black dashed lines corresponds to the distribution computed using the Lorentz factor from the simulation output, whereas the red solid lines are computed using the Terminal Lorentz factor.

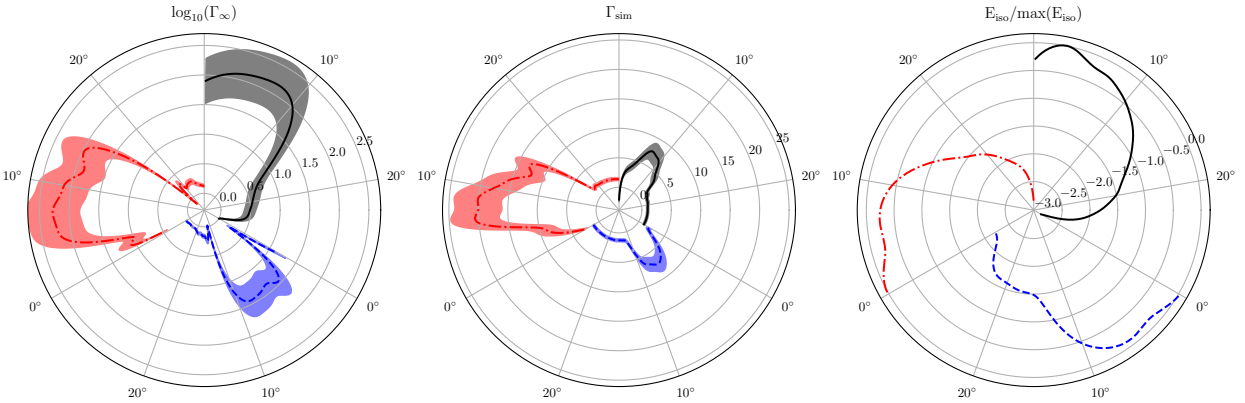


Figure 4. Left panel: Polar plot of the logarithm of the terminal Lorentz factor for the three models considered. Middle panel: Polar plot of the Lorentz factor from the simulation, Right panel: Polar plot for the energy distribution across θ . Model MHD-3D-HB is shown in black solid lines, MHD-2D-HB in red dashed-dotted lines and MHD-2D-MB in blue dashed lines. In the left and middle panels the shaded area corresponds to the $1-\sigma$ variance.

verts its magnetic energy (although the flow could also have other sources of acceleration, e.g., thermal energy) to kinetic energy and accelerates the flow (Bromberg & Tchekhovskoy 2016; Lyubarsky 2010b; Sapountzis & Vlahakis 2013). However, a consistency check is needed to verify if this acceleration is possible before the time that the outflow has started decelerating. For an outflow of an initial Lorentz factor of a few $\Gamma \gg 1$, similar to what we have from our simulations, it has been shown that the acceleration region needs to be at least 4 orders of magnitude in distance, thus taking our initial point the jet break-out, which is at around $\approx 10^8$ cm in our simulation, then the flow has efficiently accelerated at a distance of $\approx 10^{12}$ cm. For ultra-relativistic flow ($\Gamma_\infty \gg 1$) deceleration

occurs when the swept up mass, $M_{\text{sw}} = (4\pi/3)R^3 m_p n_{\text{ISM}}$ exceeds $M_{\text{ej}}(\theta)/\Gamma_\infty(\theta) = E_{\text{k,iso}}(\theta)/\Gamma_\infty^2(\theta)c^2$, where $M_{\text{ej}}(\theta)$ and $E_{\text{k,iso}}(\theta)$ are the entrained mass and the isotropic-equivalent kinetic energy of the outflow at polar angle θ . From this, we find the deceleration radius

$$r_d(\theta) = \left(\frac{3E_{\text{k,iso}}(\theta)}{4\pi m_p n_{\text{ISM}} c^2 \Gamma_\infty^2(\theta)} \right)^{1/3} \\ = 4.64 \times 10^{16} \left(\frac{E_{\text{iso}}}{4 \times 10^{51} \text{ erg}} \right)^{1/3} \times \left(\frac{\Gamma_\infty}{100} \right)^{-2/3} \left(\frac{n_{\text{ISM}}}{10^{-2}} \right)^{-1/3} \text{ cm},$$

where for the final expression we use fiducial values that are relevant

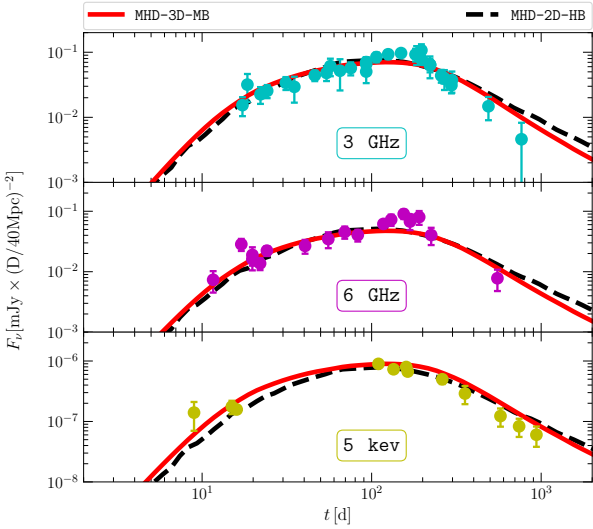


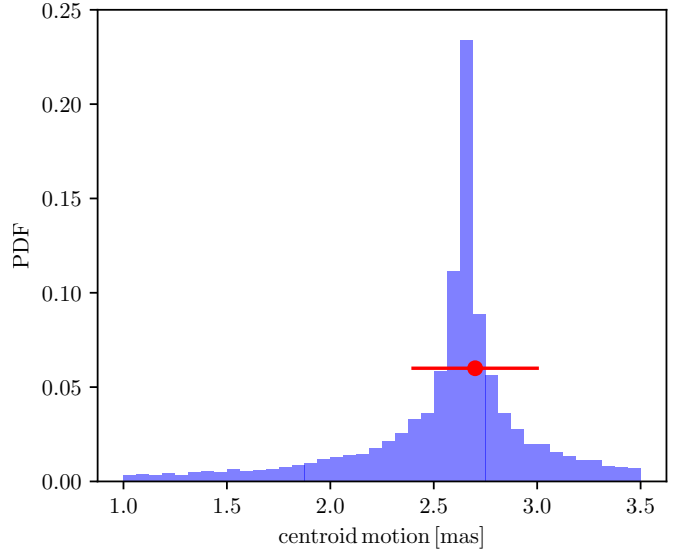
Figure 5. Left panel: Best-fit lightcurves of models MHD-3D-HB (red line) and MHD-2D-HB (dashed blue line) for the broadband afterglow observations of GRB170817A. The corner plot for the analysis to find the best-fit parameters from the genetic algorithm is shown in Fig. 6. Right panel: The distribution of the flux centroid motion for model MHD-3D-MB, the red dot with error bars correspond to the observed value for the flux centroid motion 2.7 ± 0.3 mas (Mooley et al. 2018b).

for the relativistic jet. Note that a lower Lorentz factor yields a larger r_d , thus we are confident that any acceleration occurs before the deceleration stage and use the asymptotic Lorentz factor Γ_∞ , for the calculation of the afterglow.

In the upper left and middle panels of Fig. 3 we show the distribution of the Lorentz factor, for the three models considered in Table 1, that is averaged azimuthally and extracted from the part of the outflow that reaches a radial distance $> 2 \times 10^8$ cm. In the upper left panel we present the terminal Lorentz factor Γ_∞ , computed from Eq. (1) and in the middle panel the average Lorentz factor Γ_{sim} . We find that Γ_{sim} obtained from the 3D simulation seems to be closer to that obtained from the 2D case that has a medium magnetic energy (model MHD-2D-MB). This, however, does not hold when calculating the terminal Lorentz factor as shown on the left panel of the Figure. Due to the available magnetic energy for acceleration in model MHD-3D-HB, its distribution of the terminal Lorentz factor is more similar to the high magnetic model MHD-2D-HB. In the MHD-3D-HB model the distribution of Lorentz factor (both simulation and terminal) peak at an angle $\theta \approx 8^\circ$.

In the rightmost upper panel of Fig. 3 we plot the isotropic energy of the outflow normalized with the maximum energy, due to the fact that the medium magnetic field, MHD-2D-MB has a smaller energy and it would be difficult for comparison. The maximum isotropic energies for models MHD-3D-HB, MHD-2D-HB and MHD-2D-MB are $E = 2.7 \times 10^{51}$ erg, 3.6×10^{50} erg, and 2.5×10^{49} erg respectively. In the 3D model MHD-3D-HB, the energy peaks at $\theta \approx 3^\circ$ and decreases for smaller angles. The main difference from the high magnetic model MHD-2D-HB, is that the 3D model has an extended energy distribution to larger angles till $\theta \lesssim 60^\circ$. The angular distribution of energy is similar to model MHD-2D-MB, but for this model the normalization is two orders of magnitude smaller.

In the lower panels of Fig. 3 we show the distribution of energy above a certain value of $\Gamma\beta$, i.e., $E(> \Gamma\beta)$, as a function $\Gamma\beta$, normalized by $E_{\text{iso}}(\theta)$. This energy distribution profile is approximately obtained at all polar angles. For all three models the black dashed line corresponds to the calculation performed using Γ_{sim} , whereas the red solid line corresponds to the calculation using Γ_∞ .



The energy dependence, $E(> \Gamma\beta) \propto (\Gamma\beta)^{-s}$ with $s = 4 - 5$, when using the simulation Lorentz factor is similar to the one reported in our previous work (Nathanail et al. 2020). However, assuming that acceleration is smooth and completes before any deceleration has started (as was discussed earlier) and using the terminal Lorentz factor, this dependence changes and the fast moving part of the outflow has a large amount of energy. The energy reported in Fig. 3, is measured after the jet has broken out from the merger ejecta, i.e., $t = 10$ ms.

Note that in our MHD simulations, a cut-off of $\Gamma = 20$ is set, in order to avoid parts of the outflow where the accuracy of the numerical method is reduced because of the large Lorentz factors attained.

3 AFTERGLOW EMISSION FROM THE JET

3.1 Description of the emission model

We model the afterglow emission as synchrotron radiation from shock-heated power-law electrons. The interaction of the relativistic outflow with the surrounding ISM produces a forward shock that propagates into the ISM and accelerates electrons into a power-law energy distribution, $n_e(\gamma_e) \propto \gamma_e^{-p}$, where n_e is the number density and γ_e is the Lorentz factor of the electrons. For the slope of the distribution, we employ the value $p = 2.138$, which was recently updated from the panchromatic analysis of the afterglow of GRB170817A (Makhathini et al. 2020). We further assume the standard afterglow shock microphysics where a fraction ϵ_e and ϵ_B of the total internal energy behind the shock is given to electrons and magnetic field, respectively (Sari et al. 1998).

To compute the afterglow lightcurves we use the angular distributions of the Lorentz factor and of the energy profile (cf., Fig. 3). Along the θ direction, we use 200 angles uniformly distributed to acquire the angular structure of the outflow, which then yields the initial Lorentz factor $\Gamma_0(\theta) = \Gamma_\infty(\theta)$ and the isotropic-equivalent energy $E_{\text{iso}}(\theta)$ (after MHD acceleration) of the flow. We calculate the afterglow lightcurve using a semi-analytic formalism where we

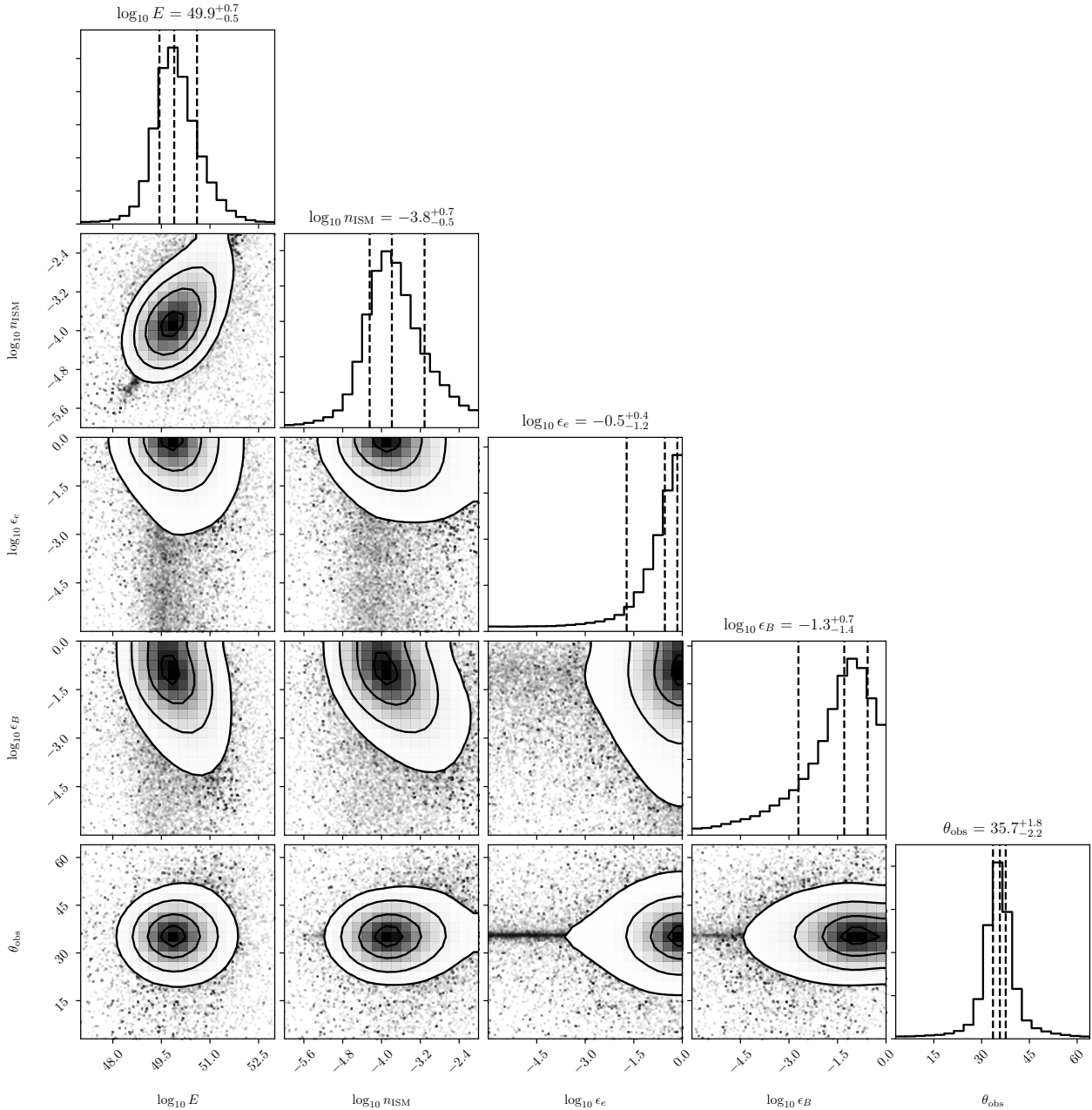


Figure 6. Corner plot from the analysis for the parameters of the best-fit lightcurves for model MHD-3D-MB, shown in Fig. 5. $1\text{-}\sigma$ uncertainties shown in the titles, are computed as the 16th and 84th percentiles of the one-dimensional posterior distribution for each parameter. The $3\text{-}\sigma$ uncertainties for the intrinsic parameters are $\log_{10} E = 49.9^{+1.6}_{-1.2}$ erg, $\log_{10} n_{\text{ISM}} = -3.8^{+1.4}_{-1.1}$ g/cm³ and $\theta_{\text{obs}} = 35.7^{+15.3}_{-17}$.

treat the flow using locally spherical dynamics for which each part of the flow expands as if it is part of a spherical flow (Granot et al. 1999; Gill & Granot 2018).

For our study, we employ the most recent afterglow data, i.e., $t \lesssim 940$ d post merger consisting of X-ray emission, optical emission and VLA radio observations (Margutti et al. 2017, 2018; Alexander et al. 2017, 2018; Hallinan et al. 2017; Mooley et al. 2018a,c; Dobie et al. 2018; Nynka et al. 2018; Troja et al. 2018, 2019; Lamb et al. 2019; Fong et al. 2019; Hajela et al. 2019; Makhathini et al. 2020). To perform the fit, we use five free parameters: the energy of the burst E , and the circum-merger density n_{ISM} , the shock microphysical parameters ϵ_e and ϵ_B , and the observer angle θ_{obs} . The model parameters outnumber the available constraints

from the data and thus the parameter space is degenerate (Gill et al. 2019b). The shape of the afterglow lightcurve near the peak can only constrain the ratio $\theta_{\text{obs}}/\theta_j$, where θ_j is the opening angle of the jet if the flow has sharp edges (for an angular structured jet this would correspond to the angular size of the relativistic core) (Nakar & Piran 2020). An additional constraint is obtained from the VLBI proper motion of the flux centroid (Mooley et al. 2018b).

To find the best-fit parameters we use a genetic algorithm to optimise the parameter selection and minimise the reduced χ^2_{ν} (Fromm et al. 2019; Nathanail et al. 2020). The fitting procedure for the lightcurve is applied to the full uniform dataset reported in Makhathini et al. (2020). Rather than fitting the observed flux in different energy bands, we first extrapolate all the observations

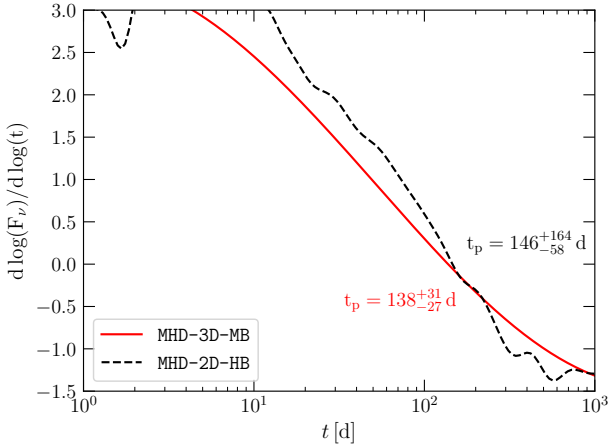


Figure 7. The slope of the best-fit lightcurves of models MHD-3D-MB (red solid) and MHD-2D-HB (dashed black). The peak of the lightcurve is reported in the plot with the 68% confidence intervals.

to a given energy, e.g., 3 GHz, and then carry out the fit to the lightcurve. This procedure is feasible since the spectrum of the broadband afterglow is described by a single power law with flux density $F_\nu \propto \nu^{-0.569}$ across all epochs (e.g., Hajela et al. 2019; Makhathini et al. 2020). Simultaneously in the fitting procedure, we require that the flux centroid motion matches the observed values³. Moreover, we assume a prior of $n_{\text{ISM}} < 0.01 \text{ cm}^{-3}$, as obtained from independent analysis of the host galaxy (Hallinan et al. 2017; Hajela et al. 2019; Makhathini et al. 2020).

The best-fit lightcurves for models MHD-3D-MB (red line) and MHD-2D-HB (dashed blue line) are shown in the left panel of Fig. 5, whereas on the right panel we show the probability distribution function for the flux centroid motion that comes from the fitting procedure. The flux centroid was calculated using the same semi-analytic formalism used to calculate the afterglow lightcurve. In particular, here we follow the prescription given in Gill & Granot (2018, see their Eq. (27)) to first form an image of the afterglow emission on the plane of the sky and then calculate the flux weighted location of the centroid. Just like the calculation of the afterglow lightcurve, this procedure relied on the input of the angular structure of the flow from the numerical simulation, namely $E_{\text{iso}}(\theta)$ and $\Gamma_\infty(\theta)$. The results of the analysis of the parameter space from the genetic algorithm is shown in the corner plot of Fig. 6. Focusing on the lightcurve, we compute the logarithmic derivative of the lightcurve in Fig. 7 for the two models MHD-3D-MB (red solid) and MHD-2D-HB (dashed black). We find that the peak of the lightcurve for both of them is consistent with observations. Overall, the afterglow lightcurve of hollow-core jet are in good agreement with the observational data from GRB170817A/GW170817 (Nathanail et al. 2020; Takahashi & Ioka 2020b,a).

3.2 Comparison with previous models

Several studies have produced lightcurves that fit the broad band afterglow observations of GW170817 and analyze the parameter

³ To obtain the correct flux centroid motion during the fitting procedure we minimise the quantity $\chi_\nu^2 + w_{fc} \times (\chi_{fc}^2 - 1)$, where χ_ν^2 comes from the lightcurve and χ_{fc}^2 from the centroid fitting, the weighting to flux centroid fitting is set to $w_{fc} = 1 - 2$.

space. Most importantly, through afterglow modelling, a better constraint for the viewing angle can be obtained, which is poorly known from the GW signal (The LIGO Scientific Collaboration & The Virgo Collaboration 2017). All methods for parameter estimation through lightcurve fitting assume hydrodynamic outflows, and the general results obtained hint to an opening angle of $\approx 3^\circ - 6^\circ$ and a observer angle of $15^\circ - 35^\circ$. The largest observer angle $\approx 35^\circ$ comes from the a 3D simulation of a structured model from (Lazzati et al. 2018), when fitting the panchromatic afterglow up to 940 d post-merger (Makhathini et al. 2020). The lowest end of the observer angle, $\approx 16^\circ$, comes from studies that fit also the VLBI constraints (Mooley et al. 2018b; Hotokezaka et al. 2019; Ghirlanda et al. 2019).

Semi-analytical calculations for a Gaussian or a power-law jet with an angular structure yield a observer angle of $\approx 20^\circ - 27^\circ$ (Resmi et al. 2018; Hotokezaka et al. 2019; Troja et al. 2019; Lamb et al. 2019; Ryan et al. 2020). The only studies that conclude to an observer angle of $> 30^\circ$ from their parameter analysis are based on hydrodynamic simulations, which however do not include the VLBI proper motion constraints (Lazzati et al. 2018; Wu & MacFadyen 2019; Hajela et al. 2019). A series of hydrodynamic simulations were used from Mooley et al. (2018b) to fit both the lightcurve and the proper motion and yielded an observer angle of $\approx 20^\circ$. Thus Makhathini et al. (2020) highlights the importance of the use of the VLBI constraints together with the uniform afterglow dataset to attain accurate estimates for the observer angle and other parameter of the outflow.

In our study we use the uniform dataset and fit the lightcurve together with the requirement for the flux centroid motion. From our analysis, presented in Fig. 6, we obtain an observer angle of $\theta_{\text{obs}} = 35.7^\circ_{-2.2}^{+1.8}$, which is the only one deduced from GRMHD simulations. It is interesting that the analysis of the afterglow with hydrodynamic outflows that use also the VLBI constraints, point to an observer angle $\theta_{\text{obs}} \approx 16$ which is far different from what we report here. The improved measurement of the observer angle from the GW is $\theta_{\text{obs}} = 29^\circ_{-15}^{+11}$ (The LIGO Scientific Collaboration et al. 2019). Analysing the GW and combining a direct measurement of the distance to the host galaxy of GW170817 yields an observer angle $\theta_{\text{obs}} = 32^\circ_{-13}^{+10}$ (Finstad et al. 2018). Using broadband photometry of the kilonova AT2017gfo associated with GW170817, results to independent constrains for the observer angle $\theta_{\text{obs}} = 32.5^\circ_{-9.7}^{+11.7}$ (Dhawan et al. 2020). All the above constraints are compatible (and in good agreement) with the MHD modelling presented in this paper.

4 AFTERGLOW EMISSION FROM THE EJECTA (KILONOVA)

The event GW170817 was followed by a kilonova detection which peaked in the ultraviolet in a few hours and in the infrared few days post merger (Arcavi et al. 2017; Nicholl et al. 2017; Chornock et al. 2017; Cowperthwaite et al. 2017; Villar et al. 2017). The modelling of this emission yielded a huge amount of r-processed neutron rich mass $\approx 0.05 M_\odot$ (Kasliwal et al. 2017; Kasen et al. 2017) that was ejected during and after the merger. This matter is expected also to produce non-thermal afterglow emission similar to what was described in Section 3. There are studies in the literature that model this emission either for the dynamical ejecta alone

(Hotokezaka et al. 2015; Radice et al. 2018) or parametrise them by prescribing a specific dependence on $\Gamma\beta$ (Kathirgamaraju et al. 2019b; Hajela et al. 2019; Troja et al. 2020).

The GRMHD outflow that we have described so far has two

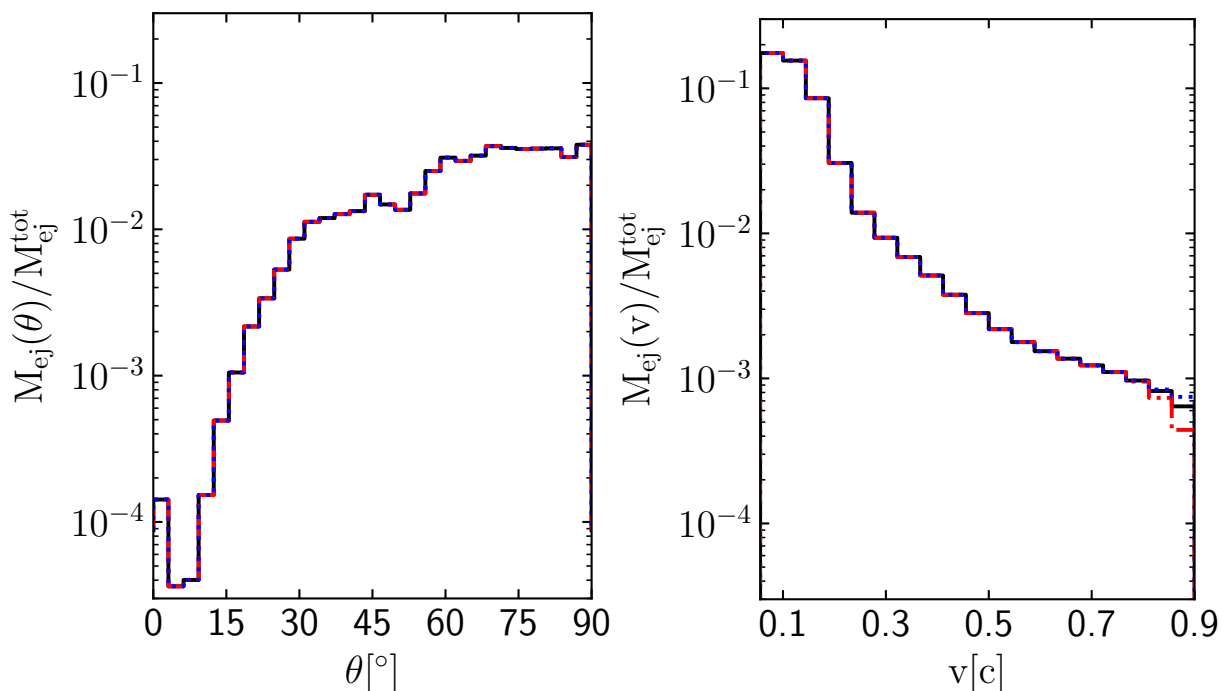


Figure 8. Normalized mass distributions for the ejected mass (MHD wind) across the angle θ (left panel) and velocity (right panel). The total amount of ejected mass from the 3D simulation is $0.027 M_{\odot}$, and it is defined as unbound matter with magnetisation $\sigma < 1$ (blue dotted), different cut-offs are shown also, Lorentz factor $\Gamma < 2$ (black solid), velocity $v < 0.82$ (red dashed).

rather distinct components: the relativistic jet confined in an angle of $\approx 15^{\circ}$ and a wide angle MHD wind that goes to very larger angles. In this Section we extract from the 3D simulation the properties of this ejected MHD wind and compute the distinct non-thermal afterglow that is expected from it. This ejected MHD wind component is matter dominated from the beginning, with $\sigma \ll 1$ as seen in Fig. 2, so no MHD acceleration is expected. We need to note that by the way the afterglow for the jet component was computed, the part of the flow that moves with a Lorentz factor of < 1.8 (upper left panel of Fig. 3), has a negligible effect on the computed lightcurve. The ejected mass that we use for the non-thermal afterglow of the kilonova, is defined as the unbound matter ($hu_t \leq -1$) that has magnetisation $\sigma < 1$ and thus is located outside of the jet. The distribution of the ejected mass applying this cut-off is shown in Fig. 8 across the angle (left plot) and the velocity (right plot). The non-thermal afterglow emission from the ejected matter (MHD wind), is calculated as discussed in the previous section but using the distribution from Fig. 8. In Fig. 9 we use the latest observations in the X-rays at 940 d post merger, to find the allowed parameter space that the emission from the ejecta component may be observed in the future. In order to find this allowed parameter space, we use the observer angle $\theta_{\text{obs}} = 35.7^{\circ}$ (see Fig. 6). The energy of the ejecta is known from the mass-velocity distribution. The ejected mass from our 3D simulation is $0.027 M_{\odot}$, and the total ejected mass inferred from kilonova modelling is up to $0.07 M_{\odot}$ (Kasen et al. 2017). Thus, we only allow the energy to vary by a factor of three, assuming that all of the ejected matter shown in the kilonova emission has the same energy distribution. For the n_{ISM} we allow a range of $-2.4 > \log_{10}(n_{\text{ISM}}) > -4.9$, which comes from $3\text{-}\sigma$ uncertainties (see Fig. 6). If future observations show a deviation

from the jet afterglow (the red solid line in Fig. 9) at very late times, this would signal the non-thermal appearance of the ejected matter, that was responsible for the thermal kilonova emission.

5 CONCLUSIONS

We have performed 3D general-relativistic MHD simulations to model the self-consistent launch of a jet after a BNS merger. Our initial configuration consists of a rotating black hole surrounded by a matter distribution that is inspired from numerical-relativity simulations where the merger process is modeled from first principles and that is meant to represent the matter ejected at the merger and till black-hole formation. We follow the evolution of the outflow beyond the break-out from the merger ejecta and use the results to extract the a self-consistent angular structure of the relativistic outflow. The outflow structure found in this way from the 3D simulation provides an important confirmation on the previous results obtained from 2D simulations, where it was shown that relativistic MHD outflows breaking out from merger ejecta have a hollow core of $\theta_{\text{core}} \approx 4^{\circ}$ and an opening angle of $\theta_{\text{jet}} \gtrsim 10^{\circ}$ (Nathanail et al. 2020).

The results of the simulations have also been used to calculate the expected non-thermal afterglow emission and to fit the panchromatic afterglow from GRB170817A that was observed between 9 – 940 d post merger (Makhathini et al. 2020). During the fitting procedure we ensure that the afterglow emission is consistent with the VLBI constraints for the superluminal motion (Mooley et al. 2018b; Ghirlanda et al. 2019). In this way, we obtain an observer

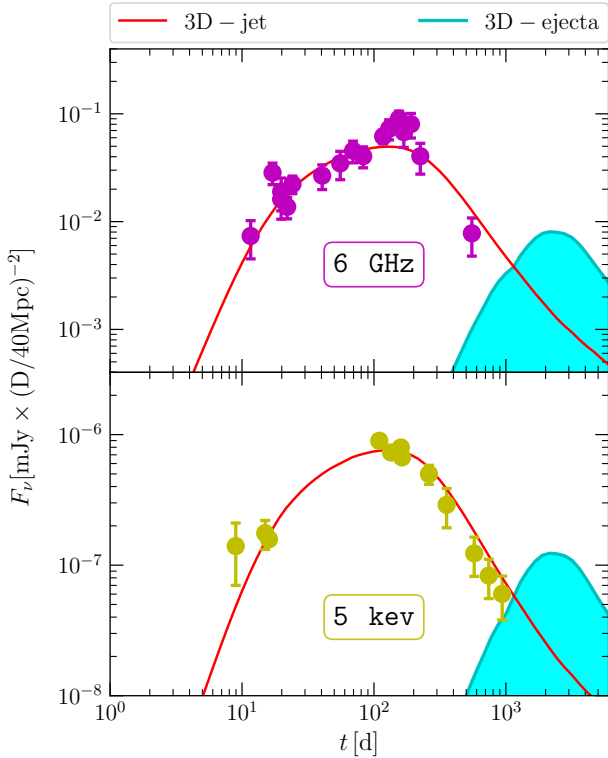


Figure 9. The jet component (red line) of model MHD-3D-MB is plotted against the broad band afterglow observations of GRB170817A, whereas the shaded cyan region corresponds to the allowed parameter space that the ejecta (kilonova) non-thermal afterglow may appear.

angle of $\theta_{\text{obs}} = 35.7^{\circ} {}^{+1.8}_{-2.2}$, consistent with independent estimations coming from GW and kilonova photometry.

The relativistic outflow in the simulations is accompanied by an MHD wind of ejected matter that is distributed with velocities of $0.05c < v < 0.9c$, with most of the ejected mass moving at $v < 0.3c$, again, a result consistent with inferences derived from kilonova observations. This component of the ejected matter is expected to give rise to a thermal emission and to produce the kilonova signal, which however we do not model in our study. On the other hand, we use the energy distribution of the ejected matter to compute the non-thermal afterglow emission that comes from the ejected matter. In this way, we conclude that this non-thermal emission from the ejected matter is potentially detectable from future observations and we provide constraints on the maximum flux density that could be expected and on the allowed parameter space for the observations.

ACKNOWLEDGEMENTS

Support comes in part also from “PHAROS”, COST Action CA16214 and the LOEWE-Program in HIC for FAIR. The simulations were performed on the SuperMUC cluster at the LRZ in Garching, on the LOEWE cluster at the CSC in Frankfurt, and on the HazelHen cluster at the HLRS in Stuttgart. RG’s research is supported by the ISF-NSFC joint research program (grant No. 3296/19).

DATA AVAILABILITY

The data underlying this article will be shared on reasonable request to the corresponding author.

REFERENCES

- Abramowicz M., Jaroszynski M., Sikora M., 1978, *Astron. Astrophys.*, **63**, 221
- Alexander K. D., et al., 2017, *Astrophys. J. Letters*, **848**, L21
- Alexander K. D., et al., 2018, *Astrophys. J. Letters*, **863**, L18
- Appl S., Lery T., Baty H., 2000, *A&A*, **355**, 818
- Arcavi I., et al., 2017, *Nature*, **551**, 64
- Baiotti L., Rezzolla L., 2017, *Rept. Prog. Phys.*, **80**, 096901
- Bauswein A., Goriely S., Janka H.-T., 2013, *Astrophys. J.*, **773**, 78
- Beniamini P., Nakar E., 2019, *Mon. Not. R. Astron. Soc.*, **482**, 5430
- Beniamini P., Petropoulou M., Barniol Duran R., Giannios D., 2019, *Mon. Not. R. Astron. Soc.*, **483**, 840
- Beniamini P., Granot J., Gill R., 2020a, arXiv e-prints, p. arXiv:2001.02239
- Beniamini P., Barniol Duran R., Petropoulou M., Giannios D., 2020b, *Astrophys. J. Lett.*, **895**, L33
- Bernuzzi S., Dietrich T., Tichy W., Brüggemann B., 2014, *Phys. Rev. D*, **89**, 104021
- Blandford R. D., Znajek R. L., 1977, *Mon. Not. R. Astron. Soc.*, **179**, 433
- Bovard L., Martin D., Guercilena F., Arcones A., Rezzolla L., Korobkin O., 2017, *Phys. Rev. D*, **96**, 124005
- Bromberg O., Tchekhovskoy A., 2016, *Mon. Not. R. Astron. Soc.*, **456**, 1739
- Bromberg O., Nakar E., Piran T., Sari R., 2011, *Astrophys. J.*, **740**, 100
- Bromberg O., Tchekhovskoy A., Gottlieb O., Nakar E., Piran T., 2018, *Mon. Not. R. Astron. Soc.*, **475**, 2971
- Chornock R., et al., 2017, *Astrophys. J. Letters*, **848**, L19
- Ciolfi R., Kastaun W., Giacomazzo B., Endrizzi A., Siegel D. M., Perna R., 2017, *Phys. Rev. D*, **95**, 063016
- Cowperthwaite P. S., et al., 2017, *Astrophys. J. Lett.*, **848**, L17
- D’Avanzo P., et al., 2018, *Astronomy and Astrophysics*, **613**, L1
- Dhawan S., Bulla M., Goobar A., Sagués Carracedo A., Setzer C. N., 2020, *Astrophys. J.*, **888**, 67
- Dietrich T., Ujevic M., Tichy W., Bernuzzi S., Brüggemann B., 2017, *Phys. Rev. D*, **95**, 024029
- Dionysopoulou K., Alic D., Rezzolla L., 2015, *Phys. Rev. D*, **92**, 084064
- Dobie D., et al., 2018, *Astrophys. J. Letters*, **858**, L15
- Duffell P. C., Quataert E., MacFadyen A. I., 2015, *Astrophys. J.*, **813**, 64
- Duffell P. C., Quataert E., Kasen D., Klion H., 2018, *Astrophys. J.*, **866**, 3
- Fernández R., Tchekhovskoy A., Quataert E., Foucart F., Kasen D., 2019, *Mon. Not. R. Astron. Soc.*, **482**, 3373
- Finstad D., De S., Brown D. A., Berger E., Biwer C. M., 2018, *Astrophys. J. Lett.*, **860**, L2
- Fishbone L. G., Moncrief V., 1976, *Astrophys. J.*, **207**, 962
- Fong W., et al., 2019, *Astrophys. J. Lett.*, **883**, L1
- Foucart F., O’Connor E., Roberts L., Kidder L. E., Pfeiffer H. P., Scheel M. A., 2016, *Phys. Rev. D*, **94**, 123016
- Fraija N., Veres P., 2018, *Astrophys. J.*, **859**, 70
- Fromm C. M., et al., 2019, *Astron. Astrophys.*, **629**, A4
- Fujibayashi S., Kiuchi K., Nishimura N., Sekiguchi Y., Shibata M., 2018, *Astrophys. J.*, **860**, 64
- Geng J.-J., Zhang B., Kölligan A., Kuiper R., Huang Y.-F., 2019, *Astrophys. J. Letters*, **877**, L40
- Ghirlanda G., et al., 2019, *Science*, **363**, 968
- Giacomazzo B., Zrake J., Duffell P. C., MacFadyen A. I., Perna R., 2015, *Astrophys. J.*, **809**, 39
- Gill R., Granot J., 2018, *Mon. Not. R. Astron. Soc.*,
- Gill R., Nathanael A., Rezzolla L., 2019a, *Astrophys. J.*, **876**, 139
- Gill R., Granot J., De Colle F., Urrutia G., 2019b, *Astrophys. J.*, **883**, 15
- Goldstein A., et al., 2017, *Astrophys. J. Letters*, **848**, L14
- Gottlieb O., Nakar E., Piran T., 2018a, *Mon. Not. R. Astron. Soc.*, **473**, 576
- Gottlieb O., Nakar E., Piran T., Hotokezaka K., 2018b, *Mon. Not. R. Astron. Soc.*, **479**, 588

- Gottlieb O., Nakar E., Bromberg O., 2020a, arXiv e-prints, p. [arXiv:2006.02466](#)
- Gottlieb O., Bromberg O., Singh C. B., Nakar E., 2020b, arXiv e-prints, p. [arXiv:2007.11590](#)
- Granot J., Piran T., Sari R., 1999, *Astrophys. J.*, **513**, 679
- Granot J., Guetta D., Gill R., 2017, *Astrophys. J. Letters*, **850**, L24
- Hajela A., et al., 2019, *Astrophys. J. Lett.*, **886**, L17
- Hallinan G., et al., 2017, *Science*, **358**, 1579
- Hamidani H., Ioka K., 2020, arXiv e-prints, p. [arXiv:2007.10690](#)
- Hamidani H., Kiuchi K., Ioka K., 2020, *Mon. Not. R. Astron. Soc.*, **491**, 3192
- Harutyunyan A., Nathanail A., Rezzolla L., Sedrakian A., 2018, *European Physical Journal A*, **54**, 191
- Hotokezaka K., Kiuchi K., Kyutoku K., Okawa H., Sekiguchi Y.-i., Shibata M., Taniguchi K., 2013, *Phys. Rev. D*, **87**, 024001
- Hotokezaka K., Kyutoku K., Okawa H., Shibata M., 2015, *Phys. Rev. D*, **91**, 064060
- Hotokezaka K., Kiuchi K., Shibata M., Nakar E., Piran T., 2018, *Astrophys. J.*, **867**, 95
- Hotokezaka K., Nakar E., Gottlieb O., Nissanke S., Masuda K., Hallinan G., Mooley K. P., Deller A. T., 2019, *Nature Astronomy*, **3**, 940
- Kasen D., Metzger B., Barnes J., Quataert E., Ramirez-Ruiz E., 2017, *Nature*, **551**, 80
- Kasliwal M. M., et al., 2017, *Science*, **358**, 1559
- Kastaun W., Galeazzi F., Alic D., Rezzolla L., Font J. A., 2013, *Phys. Rev. D*, **88**, 021501
- Kathirgamaraju A., Barniol Duran R., Giannios D., 2018, *Mon. Not. R. Astron. Soc.*, **473**, L121
- Kathirgamaraju A., Tchekhovskoy A., Giannios D., Barniol Duran R., 2019a, *Mon. Not. R. Astron. Soc.*, **484**, L98
- Kathirgamaraju A., Giannios D., Beniamini P., 2019b, *Mon. Not. R. Astron. Soc.*, **487**, 3914
- Kawamura T., Giacomazzo B., Kastaun W., Ciolfi R., Endrizzi A., Baiotti L., Perna R., 2016, *Phys. Rev. D*, **94**, 064012
- Kiuchi K., Kyutoku K., Sekiguchi Y., Shibata M., Wada T., 2014, *Phys. Rev. D*, **90**, 041502
- Kiuchi K., Cerdá-Durán P., Kyutoku K., Sekiguchi Y., Shibata M., 2015, *Phys. Rev. D*, **92**, 124034
- Kiuchi K., Kyutoku K., Sekiguchi Y., Shibata M., 2018, *Phys. Rev. D*, **97**, 124039
- Komissarov S. S., Vlahakis N., Königl A., Barkov M. V., 2009, *Mon. Not. R. Astron. Soc.*, **394**, 1182
- Lamb G. P., Kobayashi S., 2017, *Mon. Not. R. Astron. Soc.*, **472**, 4953
- Lamb G. P., Kobayashi S., 2018, *Mon. Not. R. Astron. Soc.*, **478**, 733
- Lamb G. P., Mandel I., Resmi L., 2018, *Mon. Not. R. Astron. Soc.*, **481**, 2581
- Lamb G. P., et al., 2019, *Astrophys. J. Lett.*, **870**, L15
- Lazzati D., Morsony B. J., Begelman M. C., 2010, *Astrophys. J.*, **717**, 239
- Lazzati D., López-Cámara D., Cantiello M., Morsony B. J., Perna R., Workman J. C., 2017, *Astrophys. J. Letters*, **848**, L6
- Lazzati D., Perna R., Morsony B. J., Lopez-Cámara D., Cantiello M., Ciolfi R., Giacomazzo B., Workman J. C., 2018, *Phys. Rev. Lett.*, **120**, 241103
- Lyman J. D., et al., 2018, *Nature Astronomy*,
- Lyubarsky Y. E., 2010a, *Mon. Not. R. Astron. Soc.*, **402**, 353
- Lyubarsky Y., 2010b, *Astrophys. J. Lett.*, **725**, L234
- Makhathini S., et al., 2020, arXiv e-prints, p. [arXiv:2006.02382](#)
- Margalit B., Metzger B. D., 2017, *Astrophys. J. Lett.*, **850**, L19
- Margutti R., et al., 2017, *Astrophys. J. Letters*, **848**, L20
- Margutti R., et al., 2018, *Astrophys. J. Letters*, **856**, L18
- Matsumoto J., Masada Y., 2019, *Mon. Not. R. Astron. Soc.*, **490**, 4271
- McKinney J. C., Blandford R. D., 2009, *Mon. Not. R. Astron. Soc.*, **394**, L126
- Mizuno Y., Lyubarsky Y., Nishikawa K.-I., Hardee P. E., 2012, *Astrophys. J.*, **757**, 16
- Mizuta A., Ioka K., 2013, *Astrophys. J.*, **777**, 162
- Moll R., Spruit H. C., Obergaulinger M., 2008, *A & A*, **492**, 621
- Mooley K. P., et al., 2018a, *Nature*, **554**, 207
- Mooley K. P., et al., 2018b, *Nature*, **561**, 355
- Mooley K. P., et al., 2018c, *Astrophys. J. Lett.*, **868**, L11
- Most E. R., Papenfort L. J., Rezzolla L., 2019, *Mon. Not. R. Astron. Soc.*, **490**, 3588
- Murgia-Berthier A., Montes G., Ramirez-Ruiz E., De Colle F., Lee W. H., 2014, *Astrophys. J.*, **788**, L8
- Murgia-Berthier A., et al., 2016, *Astrophys. J. Lett.*, **835**, L34
- Murgia-Berthier A., Ramirez-Ruiz E., De Colle F., Janiuk A., Rosswog S., Lee W. H., 2020, arXiv e-prints, p. [arXiv:2007.12245](#)
- Nagakura H., Hotokezaka K., Sekiguchi Y., Shibata M., Ioka K., 2014, *Astrophys. J.*, **784**, L28
- Nakar E., Piran T., 2017, *Astrophys. J.*, **834**, 28
- Nakar E., Piran T., 2020, arXiv e-prints, p. [arXiv:2005.01754](#)
- Nathanail A., 2018a, *Galaxies*, **6**, 119
- Nathanail A., 2018b, *Astrophys. J.*, **864**, 4
- Nathanail A., Porth O., Rezzolla L., 2019, *Astrophys. J. Lett.*, **870**, L20
- Nathanail A., Gill R., Porth O., Fromm C. M., Rezzolla L., 2020, *Mon. Not. R. Astron. Soc.*, **495**, 3780
- Nicholl M., et al., 2017, *Astrophys. J. Letters*, **848**, L18
- Nynka M., Ruan J. J., Haggard D., Evans P. A., 2018, *Astrophys. J. Lett.*, **862**, L19
- Olivares H., Porth O., Davelaar J., Most E. R., Fromm C. M., Mizuno Y., Younsi Z., Rezzolla L., 2019, *Astron. Astrophys.*, **629**, A61
- Palenzuela C., Liebling S. L., Neilsen D., Lehner L., Caballero O. L., O'Connor E., Anderson M., 2015, *Phys. Rev. D*, **92**, 044045
- Paschalidis V., 2017, *Classical and Quantum Gravity*, **34**, 084002
- Porth O., Olivares H., Mizuno Y., Younsi Z., Rezzolla L., Moscibrodzka M., Falcke H., Kramer M., 2017, *Computational Astrophysics and Cosmology*, **4**, 1
- Porth O., et al., 2019, *Astrophys. J. Supp.*, **243**, 26
- Pozanenko A. S., et al., 2018, *Astrophys. J. Lett.*, **852**, L30
- Radice D., Galeazzi F., Lippuner J., Roberts L. F., Ott C. D., Rezzolla L., 2016, *Mon. Not. R. Astron. Soc.*, **460**, 3255
- Radice D., Perego A., Hotokezaka K., Fromm S. A., Bernuzzi S., Roberts L. F., 2018, *Astrophys. J.*, **869**, 130
- Resmi L., et al., 2018, *ApJ*, **867**, 57
- Rezzolla L., Zanotti O., 2013, *Relativistic Hydrodynamics*. Oxford University Press, Oxford, UK, doi:10.1093/acprof:oso/9780198528906.001.0001
- Rezzolla L., Baiotti L., Giacomazzo B., Link D., Font J. A., 2010, *Class. Quantum Grav.*, **27**, 114105
- Rezzolla L., Giacomazzo B., Baiotti L., Granot J., Kouveliotou C., Aloy M. A., 2011, *Astrophys. J. Letters*, **732**, L6
- Rezzolla L., Most E. R., Weih L. R., 2018, *Astrophys. J. Lett.*, **852**, L25
- Ruiz M., Lang R. N., Paschalidis V., Shapiro S. L., 2016, *Astrophys. J. Lett.*, **824**, L6
- Ryan G., Eerten H. v., Piro L., Troja E., 2020, *Astrophys. J.*, **896**, 166
- Salafia O. S., Ghisellini G., Ghirlanda G., Colpi M., 2018, *Astron. Astrophys.*, **619**, A18
- Sapountzis K., Janiuk A., 2019, *Astrophys. J.*, **873**, 12
- Sapountzis K., Vlahakis N., 2013, *Mon. Not. R. Astron. Soc.*, **434**, 1779
- Sari R., Piran T., Narayan R., 1998, *Astrophys. J. Lett.*, **497**, L17
- Savchenko V., et al., 2017, *Astrophys. J. Letters*, **848**, L15
- Sekiguchi Y., Kiuchi K., Kyutoku K., Shibata M., Taniguchi K., 2016, *Phys. Rev. D*, **93**, 124046
- Shibata M., Fujibayashi S., Hotokezaka K., Kiuchi K., Kyutoku K., Sekiguchi Y., Tanaka M., 2017, *Phys. Rev. D*, **96**, 123012
- Siegel D. M., Ciolfi R., Harte A. I., Rezzolla L., 2013, *Phys. Rev. D*, **87**, 121302
- Siegel D. M., Ciolfi R., Rezzolla L., 2014, *Astrophys. J.*, **785**, L6
- Takahashi K., Ioka K., 2020a, arXiv e-prints, p. [arXiv:2007.13116](#)
- Takahashi K., Ioka K., 2020b, *Mon. Not. R. Astron. Soc.*, **497**, 1217
- Tchekhovskoy A., McKinney J. C., Narayan R., 2008, *Mon. Not. R. Astron. Soc.*, **388**, 551
- The LIGO Scientific Collaboration The Virgo Collaboration 2017, *Phys. Rev. Lett.*, **119**, 161101
- The LIGO Scientific Collaboration et al., 2017, *Astrophys. J. Lett.*, **848**, L12
- The LIGO Scientific Collaboration et al., 2019, *Physical Review X*, **9**, 011001

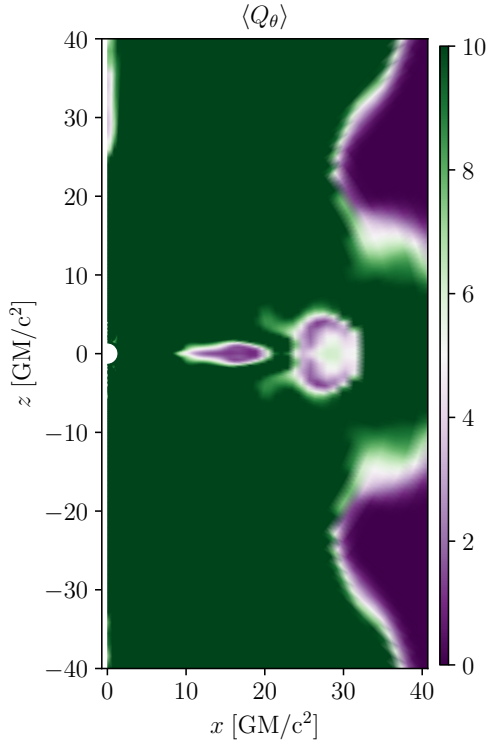


Figure A1. The MRI quality factor Q_θ in the inner regions of the accretion disc and close to the black hole.

- Troja E., et al., 2017, *Nature*, 551, 71
Troja E., et al., 2018, *Mon. Not. R. Astron. Soc.*, 478, L18
Troja E., et al., 2019, *Mon. Not. R. Astron. Soc.*, 489, 1919
Troja E., et al., 2020, *Mon. Not. R. Astron. Soc.*, 498, 5643
Urrutia G., De Colle F., Murguía-Berthier A., Ramirez-Ruiz E., 2020, arXiv e-prints, p. [arXiv:2011.06729](https://arxiv.org/abs/2011.06729)
Villar V. A., et al., 2017, *Astrophys. J. Letters*, 851, L21
Vlahakis N., Königl A., 2003a, *Astrophys. J.*, 596, 1080
Vlahakis N., Königl A., 2003b, *Astrophys. J.*, 596, 1104
Wu Y., MacFadyen A., 2019, *Astrophys. J. Lett.*, 880, L23
Xie X., Zrake J., MacFadyen A., 2018, *Astrophys. J.*, 863, 58

APPENDIX A: ON THE DEVELOPMENT OF THE MRI

As mentioned in the main text, the initial torus configuration leads to the development of the MRI and through the transfer of angular momentum drives the accretion on to the torus. Since this is an important aspect of the simulations reported here, it is important to validate that the resolution employed is sufficient to resolve properly the MRI and hence ensure that the accretion process is realistic. , thus there is the need to properly resolve the MRI inside the torus. As customary in these cases, the validation is realised in terms of the ϕ -averaged quality factor for the MRI, $Q_\theta := \lambda_\theta/dx_\theta$, where λ_θ is the wavelength of the fastest growing mode for the MRI and dx_θ the corresponding grid spacing (Porth et al. 2019). This quantity is reported in Fig. A1 as measured in the inner parts of the accretion disc and hence in the vicinity of the black hole. As indicated by the colorcode, $Q_\theta \gtrsim 10$, hence indicating that the MRI is properly resolved in the relevant region.